Article

Interfacial Electron Transfer and Synergistic Effects on NiCo(CA)@M Microbars That Boost the Alkaline Oxygen Evolution Reaction

Jiajia Liu [1], Xiao Wang [2], Yulin Min [1,3], Qiaoxia Li [1,3,*] and Qunjie Xu [1,3,*]

[1] Shanghai Key Laboratory of Materials Protection and Advanced Materials Electric Power, Shanghai University of Electric Power, Shanghai 200090, China; liujiajia@mail.shiep.edu.cn (J.L.); minyulin@shiep.edu.cn (Y.M.)
[2] School of Environmental and Chemical Engineering, Shanghai University, Shanghai 200444, China; izmski527wx@shu.edu.cn
[3] Shanghai Institute of Pollution Control and Ecological Security, Shanghai 200092, China
* Correspondence: liqiaoxia@shiep.edu.cn (Q.L.); xuqunjie@shiep.edu.cn (Q.X.)

Abstract: The development of oxygen evolution reaction electrocatalysts with a low cost, high activity, and strong stability is of great significance to the breakthrough of energy conversion technology. Herein, a composite material (NiCo(CA)@M) was obtained by growing nickel-cobalt nanoparticles on MIL-88A in situ by a simple two-step solvent thermal method. The results show that NiCo(CA)@M composite has rich active sites, and the formation of the composite induces charge redistribution between NiCo(CA) and MIL-88A, effectively reducing the reaction energy barrier, while growth in situ was conducive to the improvement of material stability. Impressively, the NiCo(CA)@M catalyst achieved a current density of 10 mA cm^{-2} in alkaline electrolyte required an overpotential of only 270 mV and the Tafel slope was 69 mV dec^{-1}. At the same time, the NiCo(CA)@M catalyst had excellent stability at a current density of 10 mA cm^{-2}, and after the 16 h i-t test, the catalyst still had 91.1% current density retention. The electrocatalytic activity did not decay significantly after 2000 CV cycles.

Keywords: electrocatalysis; water splitting; metal-organic frameworks; composite; oxygen evolution reaction

1. Introduction

The development of clean energy is of great significance to improving the energy structure, protecting the ecological environment, and realizing sustainable economic and social development [1]. Among the various clean energy sources, hydrogen energy is attracting attention as one of the most promising clean energy sources because of its high energy density, environmental friendliness, and abundant energy sources [2]. The electrolysis of water is one of the most common ways of producing hydrogen [3]. The cathodic reaction of electrolytic water is the hydrogen evolution reaction (HER), which is a relatively simple two-electron transfer process involving electrochemical H$^+$ adsorption and the desorption of H$_2$ [4]. In contrast, the oxygen evolution reaction (OER) at the anode is essentially a more complex process with slow oxygen evolution dynamics, as it requires the transfer of four electrons through a multistep reaction with single-electron transfer at each step [5]. Thus, the accumulation of energy in each step hinders the OER kinetically, and a large overpotential position is required to overcome the kinetic barrier [6]. On the other hand, OER is an important semi-reaction in rechargeable metal-air batteries [7], and it is also considered an emerging sustainable energy conversion technology [8]. However, bottlenecks such as low cycle life, poor metal stability, and limited energy conversion efficiency still limit the development of this technology [9]. Therefore, the development of highly active, inexpensive, and stable electrocatalysts for oxygen precipitation reactions

is of great importance for improving the efficiency of water electrolysis [10]. At present, precious metal oxides were considered the most advanced catalysts because of their high activity and high OER selectivity, but these catalysts have the problems of high cost, scarcity, and poor stability, so it is very necessary to develop transition metal-based materials with high activity and low costs for efficient oxygen precipitation reactions [11].

Indeed, bimetal nanoparticles have been extensively studied in recent years, as the interaction between these two components may create multiple possibilities [12]. Moreover, in the fields of catalysis, energy storage and conversion, environmental protection, and gas sensing, switching from precious metals and their oxides to the first-line transition metals of Ni, Cu, Co, Fe, and others is crucial because of the high abundance and catalytic activity potential of this group of metals [13]. In this context, bimetallic nickel–cobalt nanoparticles (NiCo NPs) have attracted social attention due to the synergistic catalytic activity of combined metals [14]. Despite the great potential of NiCo NPs in the field of catalysis, the current synthesis of NiCo NPs still faces great challenges in terms of composition, size morphology, and crystallinity with a low degree of controllability [15]. The agglomeration of nanoparticles partly limits their activity in electrochemical processes. The results show that the carbonaceous material can provide a ligand protective shell to inhibit the aggregation of nanoparticles and promote the reaction to proceed. Alternatively, the uniform distribution of nanoparticles can also reduce the agglomeration of nanoparticles [16] while introducing new active sites.

A metal-organic framework (MOF) is an inorganic–organic hybrid material with intramolecular pores composed of metal ions (or clusters) and organic ligands [17]. It has a large number of unsaturated metal coordination centers, a highly tunable structure, and a large specific surface area, which has attracted a lot of attention in the field of electrolytic water [18]. Some of the literature has reported the direct use of various types of MOF materials for oxygen evolution reactions [19], but unfortunately, the results showed that the catalysts of this class are severely limited in their OER activity due to their ultra-low conductivity, and the inherent catalytic activity of MOFs materials needs to be further enhanced [20]. Currently, MOF materials are usually used as sacrificial templates or annealed as precursors for conversion to derivative materials [21]. In recent years, some research results have shown that metal-organic frameworks have good potential as carriers for non-precious metal catalysts to enhance their catalytic activity [22], which is attributed to the formation of multiphase interfaces that not only improve the electronic interactions between materials, but also enhance chemical stability, promote the generation of highly active substances, or modulate the reaction intermediates in catalyst surface chemisorption (*O, **OH, * OOH), promoting OER [23]. At the same time, the orbital electronic interactions between different metals can cause subtle atomic arrangements, which can change the chemical ring of iron-based electrocatalysts [24]. Specifically, the rational tuning of the three-dimensional electronic structure provides good adsorption/desorption of oxygen-containing intermediates for iron-based electrocatalysts [25]. For example, Yaqoob et al. [26] produced an iron–nickel 2-amioterephthalic acid metal-organic framework (FeNiNH$_2$BDC MOF) using a simple solvothermal method and compounded it with 2~6 wt% carbon nanotubes (CNTs). Based on the synergistic effect of the bimetallic organic backbone MOF and conductive carbon nanotubes, the obtained composites exhibited excellent electrocatalytic behavior during the oxygen precipitation reaction (OER) in an alkaline medium.

In this work, we have grown nickel–cobalt nanoparticles in situ on the surface of a metal-organic framework (defined as NiCo(CA)@M) using a simple solvothermal method and used them as efficient OER catalysts. On the one hand, this in situ growth effectively reduces the agglomeration of nanoparticles and enhances the corrosion resistance of the catalyst, while introducing new active sites and increasing the active specific surface area. On the other hand, the formation of the composite induces electron transfer between the nickel–cobalt nanoparticles and the metal-organic backbone, and this charge redistribution can effectively reduce the reaction energy barrier. The catalytic activity of the composite

material was significantly enhanced for the alkaline oxygen precipitation reaction, and the stability was excellent.

2. Materials and Methods

2.1. Reagents and Materials

Cobalt nitrate hexahydrate ($Co(NO_3)_2 \cdot 6H_2O$, 99%), nickel nitrate hexahydrate ($Ni(NO_3)_2 \cdot 6H_2O$, 99%), and citric acid monohydrate (CA, analytical pure) were purchased from Adamas Reagent Co., Ltd., Shanghai, China. The used iron chloride hexahydrate ($FeCl_3 \cdot 6H_2O$, 99%), N, N-dimethylformamide (DMF, 99%), Fumaric acid ($C_4H_4O_4$, 99%), and isopropyl alcohol (C_3H_8O, 99.5%) were all obtained from Shanghai Titan Technology Co., Ltd., Shanghai, China. Triethylamine (TEA) and ethanol (C_2H_6O, analytical pure) were purchased from Sinophol Chemical Reagent Co., Ltd. (Shanghai, China) We purchased Nafion® solution (5 wt% by weight) from DuPont (Wilmington, DE, USA). All the chemicals were used directly after the purchase without any purification.

2.2. Synthesis of MIL-88A

Notably, 139.3 mg of fumaric acid was dispersed in deionized water (DI), and then 525.2 mg of $FeCl_3 \cdot 6H_2O$ was added while stirring continuously at 70 °C for 10 min. Then, the orange solution we obtained (as mentioned above) was transferred to a stainless-steel autoclave containing Teflon liner for hydrothermal reaction and stored at 110 °C for 6 h. Subsequently, it was cooled to room temperature, and the orange precipitate MIL-88A was obtained by means of centrifugation and was washed three times with DI.

2.3. Synthesis of Ni(CA), Co(CA), and NiCo(CA)

Moreover, 580 mg of $Ni(NO_3)_2 \cdot 6H_2O$ was added to a transparent reagent bottle containing 20 mL of DMF and was magnetically stirred until fully dissolved. Subsequently, 420 mg of monohydrate citric acid and 1 mL of triethylamine were added to the solution with magnetic stirring for 12 h. Then, the mixed solution was stirred at 80 °C for 1 h. After the reaction, the product was collected by means of centrifugation and washed three times with DMF. After the centrifugation process, the obtained catalyst was dried in a vacuum oven at 60 °C to obtain Ni(CA).

Co(CA) was prepared in the same way as Ni(CA), the only difference being the substitution of the metal source, the replacement of $Ni(NO_3)_2 \cdot 6H_2O$ in the above reaction with $Co(NO_3)_2 \cdot 6H_2O$, and keeping the rest of the steps the same.

The process of preparing NiCo(CA) is the same as described above, except that 465 mg of $Ni(NO_3)_2 \cdot 6H_2O$ and 84 mg of $Co(NO_3)_2 \cdot 6H_2O$ were added in the first step of preparing NiCo(CA).

2.4. Synthesis of Ni(CA)@M, Co(CA)@M, and NiCo(CA)@M

Notably, 30 mg of the synthesized MIL-88A was taken and dispersed in 10 mL of DMF, and 10.13 mg of $Ni(NO_3)_2 \cdot 6H_2O$ and 2.53 mg of $Co(NO_3)_2 \cdot 6H_2O$ were added. After magnetic stirring for 30 min, 9.14 mg of monohydrate citric acid and 1 mL of triethylamine were added successively, and magnetic stirring was continued for 12 h. The mixture reacted at 80 °C for 1 h. Subsequently, it was cooled to room temperature, and the orange powder NiCo(CA)@M was collected by means of a centrifugation process, washed 3 times with DMF, and dried in a vacuum oven.

For comparison, a similar approach was taken to prepare the Ni(CA)@M and Co(CA)@M. When preparing Ni(CA)@M, 12.66 mg $Ni(NO_3)_2 \cdot 6H_2O$ was added, and the other steps were consistent with those mentioned above. Notably, 12.66 mg $Co(NO_3)_2 \cdot 6H_2O$ was added in the first step of preparing Co(CA)@M, and other steps were consistent with the above-mentioned steps.

2.5. Instruments and Characterization

Micromorphology was characterized by means of scanning electron microscopy (SEM, Regulus8100, Hitachi Ltd., Tokyo, Japan), transmission electron microscopy (TEM, JEM-2100 PLUS, JEOL Ltd., Tokyo, Japan), and high-resolution transmission electron microscopy (HRTEM, JEM-2100 PLUS, JEOL Ltd., Tokyo, Japan). X-ray diffraction (XRD) analysis was performed using a D8 Advance X-ray diffractometer from Bruker (Leipzig, Germany). X-ray diffraction characterization was performed to obtain crystal structure information concerning the material using Cu-K$_\alpha$ as the radiation source. The instrument model used for the Fourier Transform Infrared Spectroscopy (FTIR) analysis was the Thermo Scientific NicoletiS10 FT-IR spectrometer (Thermo Fisher, Waltham, MA, USA). For X-ray photo-electron spectroscopy (XPS) analysis, the ESCALAB 250 X-ray electron spectrometer was produced by Thermo Fisher (Waltham, MA, USA), using monochrome Cu (K$_\alpha$ = 1486.6 eV) X-ray as the excitation source.

2.6. Electrochemical Measurements

The catalyst ink was prepared as follows: For the powder catalyst, 5 mg of the sample was weighed and dispersed in a 1 mL solution composed of 780 µL of isopropanol, 200 µL of DI, and 20 µL Nafion solution. Then, the above solution was mixed using ultrasound for 30 min to form a well-dispersed ink. Subsequently, 10 µL of the catalyst ink was pipetted on a polished glassy carbon electrode. After natural drying, the working electrode with a load of 0.255 mg cm^{-2} was obtained.

All electrochemical performance tests were performed at the CHI 660E electrochemical workstation in Chenhua, Shanghai, using a standard three-electrode system. The test was performed in a 1 M potassium hydroxide solution saturated at room temperature using the US rotating disc ring electrode device (RDE, PINE research instrument, Princeton, NJ, USA) with a total speed of 1600 rpm. In the three-electrode system, the working electrode was the glass carbon electrode supported by the catalyst, the relative electrode was the graphite rod, and the reference electrode was the Ag/AgCl electrode. For convenience, it was not specified in this paper that the voltage mentioned was that of a relatively reversible hydrogen electrode (RHE). The measured voltage (relative to the Ag/AgCl electrode) was calibrated using the Nernst equation: $E_{RHE} = E_{Ag/AgCl} + E^\theta{}_{Ag/AgCl}(0.197\ V) + 0.059 \times pH$. E_{RHE} was the calibrated relative reversible hydrogen electrode voltage, $E_{Ag/AgCl}$ was the measured voltage (relative Ag/AgCl electrode), and $E^\theta{}_{Ag/AgCl}$ is the standard electrode voltage of Ag/AgCl.

All polarization curves of LSV were compensated with 90% iR. The measured current density j was obtained using the geometric area normalization of the glassy carbon electrode (Φ = 5 mm). Based on the obtained linear scan voltametric curve (LSV), the Tafel slope was determined according to $\eta = a + b \times \log|j|$ fitting, where η was the overpotential ($\eta = E_{RHE} - 1.23\ V$), j was the current density, and b is the Tafel slope. Cyclic voltammetry (CV) curves were measured in the potential range of 1.1~1.2 V at scanning rates of 10, 20, 30, 40, and 50 mV s^{-1}, respectively. The electrochemical bilayer capacitance (C_{dl}) was measured by measuring a cyclic voltametric curve (CV) at non-Faraday areas in the potential range of 1.1 to 1.2 V at scan rates of 10 to 50 mV s^{-1}. The linear fit of the current density difference ($\Delta j/2 = (j_{anodic} - j_{cathodic})/2$) at 1.15 V elucidated the slope C_{dl}, and the electrochemical active surface area (ECSA) was proportional to C_{dl}. The electrochemical impedance spectrum (EIS) was obtained by testing at a voltage of 1.5 V (vs. RHE) and a scanning frequency range of 0.1 Hz to 100 kHz. The equivalent circuit model was also determined by means of fitting with the Zview-Impedance software (Scribner Associates, Inc., 2.9.0.11).

3. Results and Discussion

3.1. Structure of NiCo(CA)@M Composite Material

NiCo(CA)@M micro sticks were synthesized according to the experimental flow and design ideas shown in Scheme 1. Firstly, FeCl$_3$·6H$_2$O was dispersed in deionized water

containing fumaric acid and then underwent a hydrothermal reaction to generate the metal-organic frame (MIL-88A). Subsequently, we took parts of the metal-organic framework dispersed in DMF and added cobalt nitrate and nickel nitrate. Through a cation exchange reaction, part of the nickel source and cobalt source became fixed to the MIL-88A instead of iron atoms. After that, the citric acid (CA) as a ligand was added to coordinate with the nickel and cobalt ion and the complexation reaction through solvent heat, and the nickel–cobalt nanoparticles were grown in situ on the MOF to achieve the purpose of dispersing the nickel–cobalt nanoparticles.
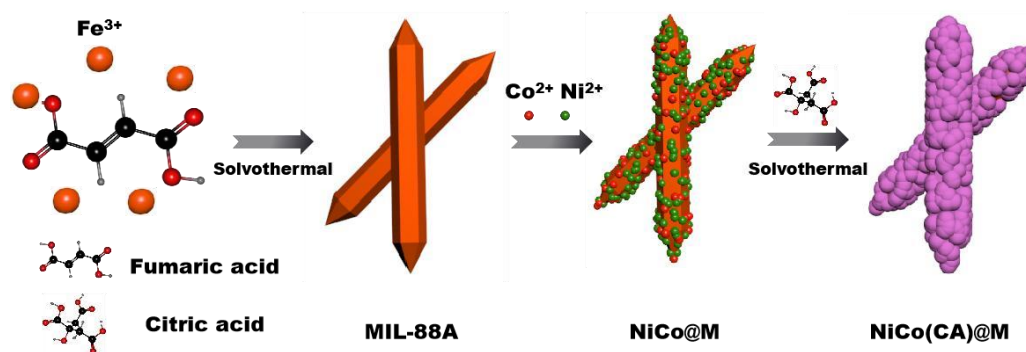
Scheme 1. The schematic synthetic route for NiCo(CA)@M.

The microscopic morphological structures of MIL-88A, NiCo(CA), and NiCo(CA)@M catalysts were observed by means of SEM and HRTEM. As shown in Figure 1a,c, MIL-88A was visible as a spindle with a size of about 2.5 μm and a smooth and neat surface. As can be seen from Figure 1b,d, the combination of the metal-organic framework with the nickel–cobalt nanoparticles increased the spindle structure width of the composite (NiCo(CA)@M) from 300 nm to 600 nm, and reduced the spindle surface smoothness compared with pure MIL-88A, which can be seen from the edge parts of NiCo(CA)@M. As can be seen from the locally enlarged TEM diagram of NiCo(CA)@M (Figure S1), the substance loaded on the metal-organic skeleton belongs to the nickel–cobalt nanoparticles, which is a zero-dimensional material. In NiCo(CA)@M, there was a clear interface between the nickel–cobalt nanoparticles and the metal-organic framework, which is predicted from the structure and belongs to a 0D/3D interface. Moreover, the TEM/EDS analysis of Figure 1e showed that the citric acid-ligated nickel–cobalt nanoparticles are loaded on the backbone of MIL-88A, the elements Ni and Co are uniformly distributed in the hierarchical structure of the MIL-88A shell surface, and MIL-88A were well wrapped, which further proved that the zero-dimensional nickel–cobalt nanoparticles were successfully grown on the spindle-shaped structure of the MIL-88A surface. The elemental analysis spectrum and elemental analysis results of NiCo(CA)@M were shown in Figure S2 and Table S1, respectively.

The X-ray diffraction (XRD) patterns of the synthesized NiCo(CA)@M and MIL-88A are shown in Figure 2a. The derivative peaks of the synthesized MIL-88A correspond to the typical crystal structure that MIL-88A has ($2\theta \approx 7.5, 10.2, 13.1, 14.5°$) [27], and the corresponding diffraction peaks of the catalyst NiCo(CA)@M were also present at $2\theta \approx 7.5, 10.2, 13.1,$ and $14.5°$, but the peaks were weaker compared to the pure MIL-88A because the outer layer of the metal-organic framework loaded a layer of nickel–cobalt nanoparticles, which affected the MIL-88A peak appearance [28]. The bonding structures of the synthesized catalysts MIL-88A and NiCo(CA)@M were determined using Fourier Transform Infrared Spectroscopy (FTIR). As observed in Figure 2b, both pure MIL-88A and NiCo(CA)@M showed a broad band around 3401 cm^{-1}, which for pure MIL-88A can be attributed to the adsorption of water molecules on the surface of this catalyst, and for the composite NiCo(CA)@M, which corresponded to the -OH stretching vibration inherent in the citric acid structure and the adsorption of airborne water molecules. For pure MIL-88A, the absorption peaks located at 1388 and 1550 cm^{-1} in the figure were attributed to the

symmetric and asymmetric stretching vibrations of the -COO$^-$ group in the iron-metal-organic ligand (fumaric acid), and the absorption peak at 1667 cm^{-1} can be attributed to the stretching vibration of the -C=C- bond in the metal-organic backbone [29]. Meanwhile, the absorption peak appearing at 595 cm^{-1} belonged to the Fe-O stretching vibration of the Fe$_3$(μ_3)O node produced by Fe-O stretching vibrations [30], indicating the vibration of the coordination bond between the carboxyl group and the metal center in the organic ligand. The above results indicated the successful synthesis of MIL-88A [31].
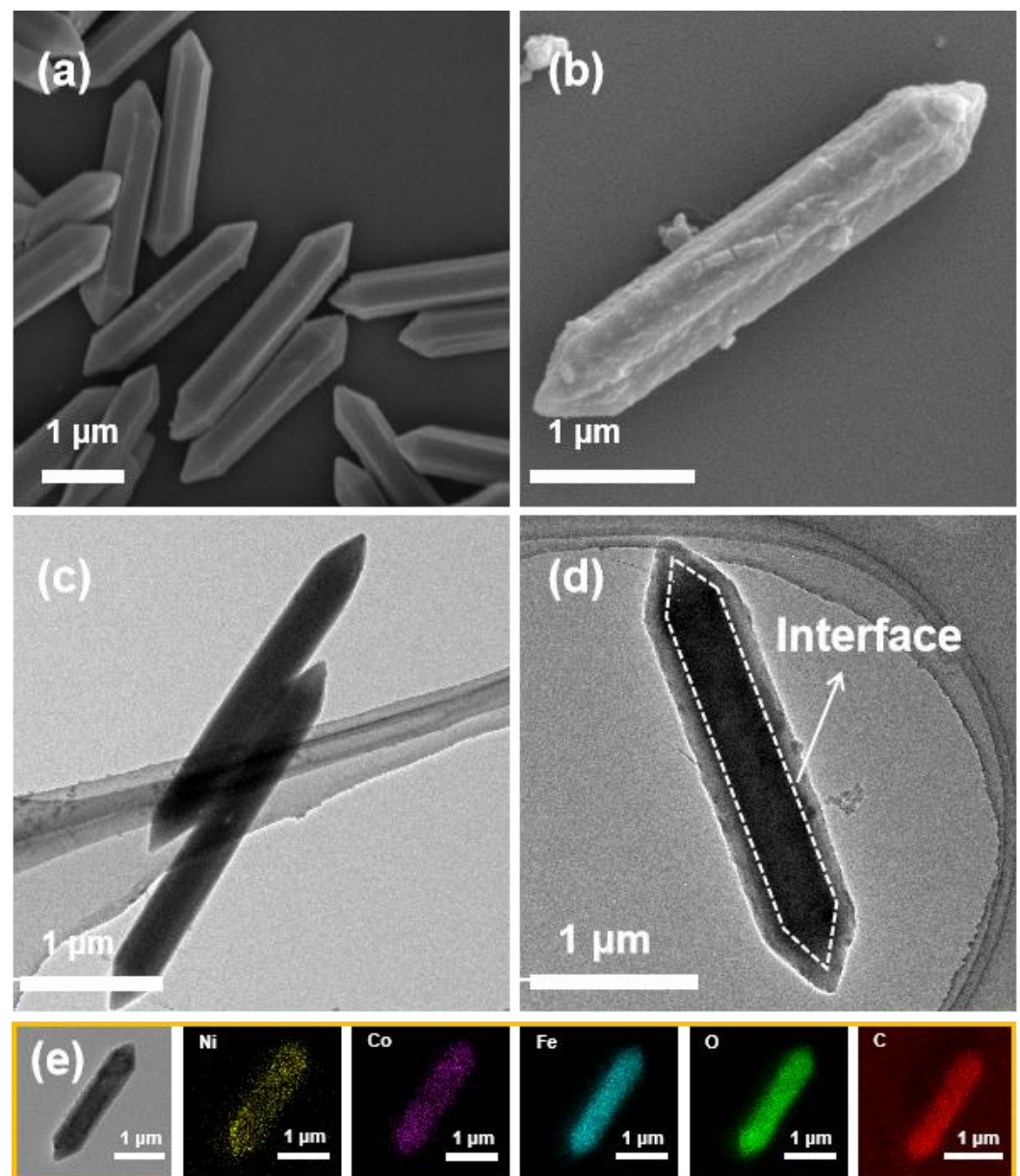

Figure 1. SEM images of (**a**) MIL-88A and (**b**) NiCo(CA)@M. TEM images of (**c**) MIL-88A and (**d**) NiCo(CA)@M. (**e**) HRTEM images and elemental mapping of NiCo(CA)@M: yellow, purple, blue, green, and red indicated the distribution of nickel, cobalt, iron, oxygen, and carbon elements, respectively.
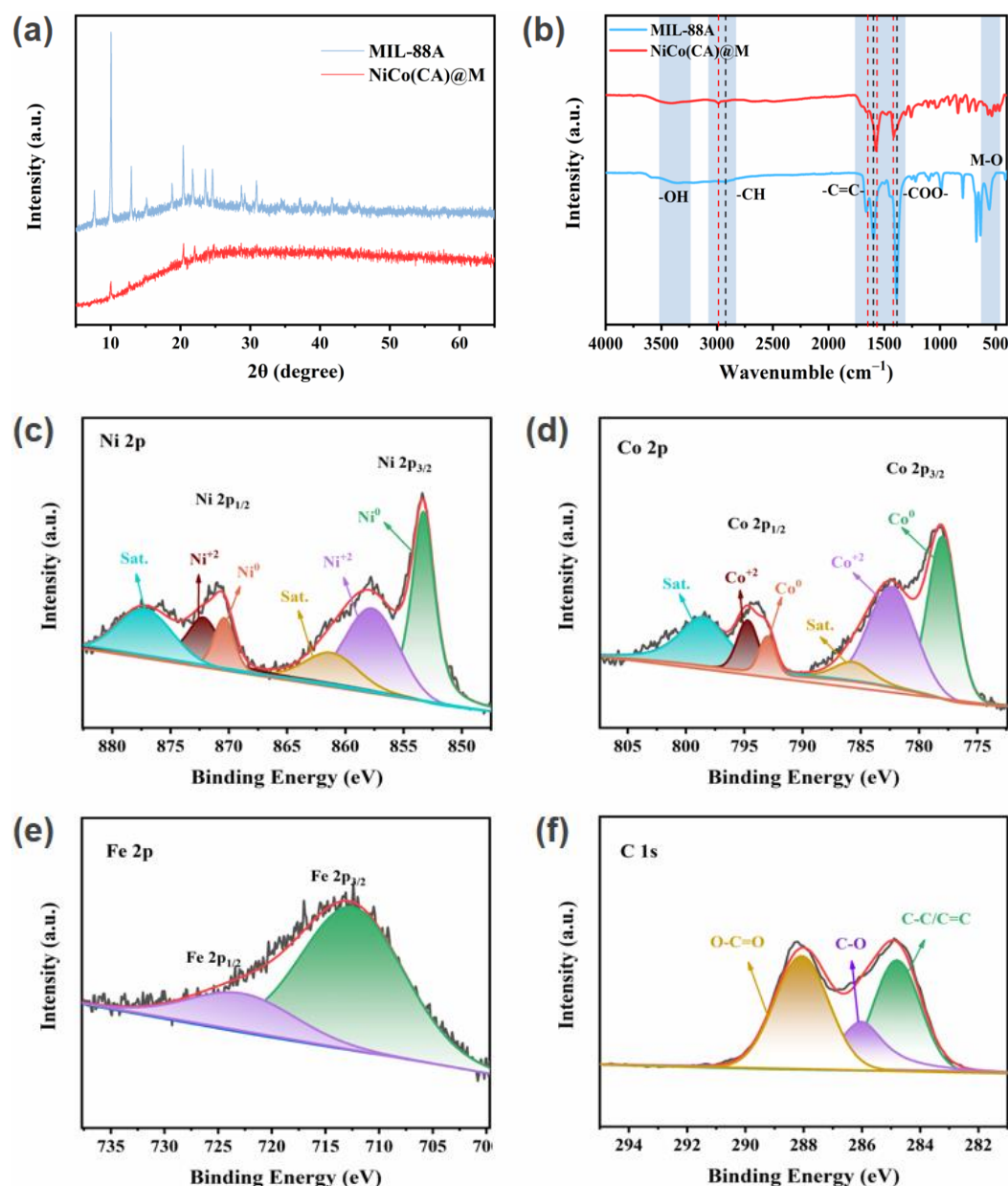
Figure 2. (**a**) XRD of the MIL-88A and NiCo(CA)@M. (**b**) FTIR spectra of NiCo(CA)@M. XPS spectra of the NiCo(CA)@M: (**c**) Ni 2p; (**d**) Co 2p; (**e**) Fe 2p; and (**f**) C 1s.

For NiCo(CA)@M, the absorption band located around 2988 cm^{-1} in the FTIR diagram was the C–H bond, which can be attributed to the C–H bond in the citric acid in the nanoparticles. The two distinct absorption peaks located at 1415 and 1575 cm^{-1} were attributed to symmetric and asymmetric stretching vibrations of the carboxylic acid [32] in the citric acid ligand. Moreover, the frequencies of these two absorption peaks in the composite are lower than those of the free citric acid, further indicating their coordination with nickel and cobalt. The peak around 534 cm^{-1} corresponds to the M–O bond, which in the composite indicates the presence of coordination bonds between Ni, Co, and O [33]. Meanwhile, it was noteworthy that no typical absorption peaks belonging to undissociated carboxyl groups were found in the 1700~1720 cm^{-1} region in both pure MIL-88A and the composite, suggesting that each carboxyl group in the nickel–cobalt nanoparticles and the metal-organic backbone were deprotonated [34].

The chemical states of the surface elements of NiCo(CA)@M catalysts as well as the complexation were analyzed using the XPS method. The full measurement spectrum

revealed the co-existence of the Ni, Co, Fe, C, and O components in the NiCo(CA)@M (Figure S3). As shown in Figure 2c, the XPS spectra of Ni 2p of NiCo(CA)@M belong to Ni $2p_{3/2}$ and Ni $2p_{1/2}$ peaks located at 853.4 and 870.6 eV, respectively, and satellite peaks at 861.4 and 879.6 eV. The two peaks obtained in the Ni $2p_{3/2}$ spectrum at 853.40 and 855.63 eV correspond to the metal state Ni^0 and the oxidation states Ni^{2+}, respectively, by deconvolution [35]. The two peaks obtained in the Ni $2p_{1/2}$ spectrum at 870.4 and 872.3 eV were attributed to the metal state Ni^0 and the oxidation states Ni^{2+}, respectively. Figure 2d showed the XPS spectrum of Co 2p, where the characteristic peaks of NiCo(CA)@M at 778.1 eV and 794.7 eV were assigned to Co $2p_{3/2}$ and Co $2p_{1/2}$ [36], respectively. In addition, the Co $2p_{3/2}$ peaks at 778.6 eV and 781.4 eV correspond to the metallic Co^0 and oxidation states Co^{2+}, and the two peaks obtained in the Co $2p_{1/2}$ spectrum at 793.0 eV and 794.7 eV belonged to metal state Co^0 and the oxidation states Co^{2+}, respectively. The two observed satellite peaks are located at 785.2 and 802.5 eV [37]. Moreover, in the NiCo(CA)@M, the signal of Fe 2p was weaker (Figure 2e). The characteristic peaks located at 713.1 eV were attributed to Fe $2p_{3/2}$, with a broad peak associated with the LMM Auger transition of Co, which is due to the lack of distribution of Fe species in the outermost layer and further indicated the successful loading of nanoparticles in the outer layer of MIL-88A [38]. Figure 2f showed the XPS spectra of C 1s at 284.8 eV (non-oxygenated carbon: C-C) and 289.3 eV (oxygenated carbon: C-O) and the 286.0 eV (carboxylated carbon: O=C-O) peaks that correspond well to the three carbon components in the NiCo(CA)@M [39].

After NiCo(CA) was compounded with MIL-88A, the binding energy positions of Ni $2p_{3/2}$ and Co $2p_{3/2}$ peaks were shifted to a certain degree compared with the pure nickel cobalt. The characteristic peak of Ni $2p_{3/2}$ shifted by 0.81 eV towards the high binding energy direction, and the characteristic peak position of Co $2p_{3/2}$ shifted to the low binding energy direction by 0.43 eV. The peak of carboxylate C 1s moved toward the low binding energy of 0.15 eV. Meanwhile, compared to pure MIL-88A, the binding energy position of Fe $2p_{3/2}$ in NiCo(CA) increased by 0.3 eV. It was shown that there is not only electron transfer from nickel to cobalt, but also charge redistribution between the nickel–cobalt nanoparticles and the metal-organic framework in the composite material [40] after the complex hybridization of MIL-88A with NiCo(CA). In the composites, the peak intensity of the nickel-oxidation state of nickel in XPS was highly enhanced compared to the metallic state of nickel, indicating an increase in the concentration of oxidation state nickel in the composites. Meanwhile, the high-resolution spectra of C 1s of NiCo(CA)@M showed that the introduction of citric acid-linked nickel–cobalt nanoparticles effectively increased the concentration of carboxylated carbon and the characteristic peak of carboxylated carbon shifted to a low binding energy. This interfacial electron transfer between the metal-organic backbone and nickel–cobalt nanoparticles could effectively accelerate the reaction process. The results show that NiCo(CA) and MIL-88A promote the electron transfer in NiCo(CA)@M, thus enhancing the intrinsic activity of OER.

3.2. OER Activity and Stability of the NiCo(CA)@M Catalyst

Electrochemical tests were performed on this type of catalyst using a three-electrode system at 1 M KOH to investigate the OER activity of different catalysts. The LSV polarization curves are shown in Figure 3a. The LSV curve of the carrier MIL-88A shows poor OER activity (η_{10} = 402 mV), which is fundamentally due to the high impedance of the metal-organic framework. The composite NiCo(CA)@M has an optimal OER activity compared to the corresponding catalyst, requiring only 270 mV overpotential to reach 10 mA cm^{-2} (η_{10} = 270 mV), while the η_{10} for MIL-88A, Ni(CA), Ni(CA)@M, NiCo(CA)@M, Co(CA)@M, and Co(CA) were 402, 484, 296, 337, and 397 mV, respectively, and thus indicated that NiCo(CA)@M had excellent OER activity. To compare the differences in overpotentials more visually, histograms of overpotentials were plotted as shown in Figure 3b to illustrate the effect of loaded nickel–cobalt nanoparticles on OER activity. The overpotential of NiCo(CA)@M at 10 mA cm^{-2} was compared with the previously reported electrocatalysts for OER activity as shown in Table S3, which was superior to that of CoMo-

MI-600 (η_{10} = 316 mV) [41], Co-Fe-BDC (η_{10} = 295 mV) [42], NiFe-MOF (η_{10} = 390 mV) [43], NiCoP/NF (η_{10} = 370 mV), [44] and UTSA-16 (η_{10} = 408 mV) [36]. The results showed that the composite NiCo(CA)@M had a smaller overpotential than the pure MIL-88A and the pure nanoparticles. Apparently, the reasonable loading of nanoparticles on the metal skeleton helped to introduce new active sites and reduced agglomeration, and the rough surface exposing additional active sites may also provide more channels to accelerate electron transport. At the same time, both the synergistic effect [45] between the transition metals and the charge redistribution within the composite contributed to the intrinsic activity of the catalyst.
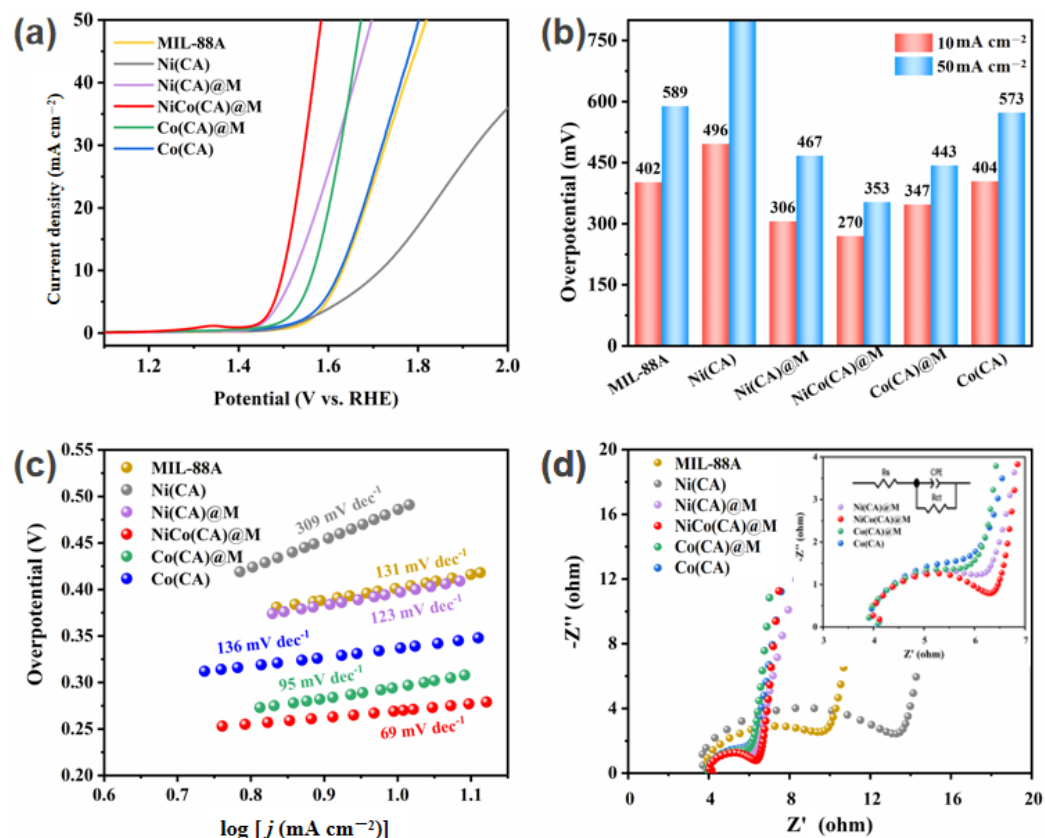

Figure 3. (**a**) LSV curves of MIL-88A, Ni(CA), Ni(CA)@M, NiCo(CA)@M, Co(CA)@M, and Co(CA) at 1 M KOH. (**b**) Comparison of the overpotentials at j = 10 mA cm^{-2} and j = 50 mA cm^{-2}. (**c**) Tafel slopes corresponding to MIL-88A, Ni(CA), Ni(CA)@M, NiCo(CA)@M, Co(CA)@M, and Co(CA) are obtained from the LSV curve. (**d**) Nyquist diagram of MIL-88A, Ni(CA), Ni(CA)@M, NiCo(CA)@M, Co(CA)@M, and Co(CA), with the Nyquist diagram amplification and fitting of Ni(CA)@M, NiCo(CA)@M, Co(CA)@M, and Co(CA).

To further determine its catalytic activity, the Tafel slope was further calculated and processed based on the obtained LSV polarization curves, and the reaction kinetics of its oxygen evolution reactions were evaluated by means of the Tafel slope [46]. As shown in Figure 3c, the Tafel slopes of MIL-88A, Ni(CA), Ni(CA)@M, Co(CA)@M, and Co(CA) were 131, 309, 123, 95, and 136 mV dec^{-1}, respectively, in the corresponding overpotential region. The lower Tafel slope of 69 mV dec^{-1} for NiCo(CA)@M in the overpotential region of 250~285 mV indicates that the hydroxide or hydroxyl oxide generated during the reaction is very fast in the interface between nickel–cobalt nanoparticles and MIL-88A, which can be attributed to the change in its decisive step, elucidating that the introduction of the nickel–cobalt nanoparticles significantly improves the electronic conduction. In comparison with other samples, NiCo(CA)@M has a more rapid OER kinetics, and the results are consistent with the EIS test. As shown in Figure 3d, the R_{ct} of NiCo(CA)@M was 2.255 Ω. The

composite materials all possess a smaller R_{ct} than the single parent (Table S2), which was affiliated with the catalyst composite's interfacial interaction, which facilitates the accelerated charge transfer between NiCo(CA)@M and the electrode/electrolyte to improve the conductivity. In addition, the Rct of Ni(CA)@M and Co(CA)@M were 2.510 and 2.620 Ω, respectively, indicating that NiCo(CA)@M has the lowest resistance value compared to other catalysts and suggesting that NiCo(CA)@M has excellent electron transfer capability in alkaline media.

The bilayer capacitance C_{dl} is theoretically positively correlated with the value of the electrochemical surface area (ECSA). Herein, cyclic voltammetry (CV) was chosen to test the cyclic voltammetry curves of the catalysts located in the non-Faraday region at different sweep rates, and the bilayer capacitance (C_{dl}) of this type of catalysts was calculated to evaluate the electrochemically active surface area (ECSA). Figure 4a–f show the CV curves of MIL-88A, Ni(CA), Ni(CA)@M, NiCo(CA)@M, Co(CA)@M, and Co(CA), respectively. The results are shown in Figure 4g, and the C_{dl} value for NiCo(CA)@M was 5.90 mF cm^{-2}, above Ni(CA)@M (4.70 mF cm^{-2}) and Co(CA)@M (4.11 mF cm^{-2}). Even 73.75,49.16 and 15.95 times of Ni (CA) (0.08 mF cm^{-2}), MIL-88A (0.12 mF cm^{-2}) and Co(CA) (0.37 mF cm^{-2}), respectively, indicated that NiCo(CA)@M had a larger activity surface area and also demonstrated that proper loading of nickel-cobalt nanoparticles on MOF can effectively increase or expose more catalytic active sites.
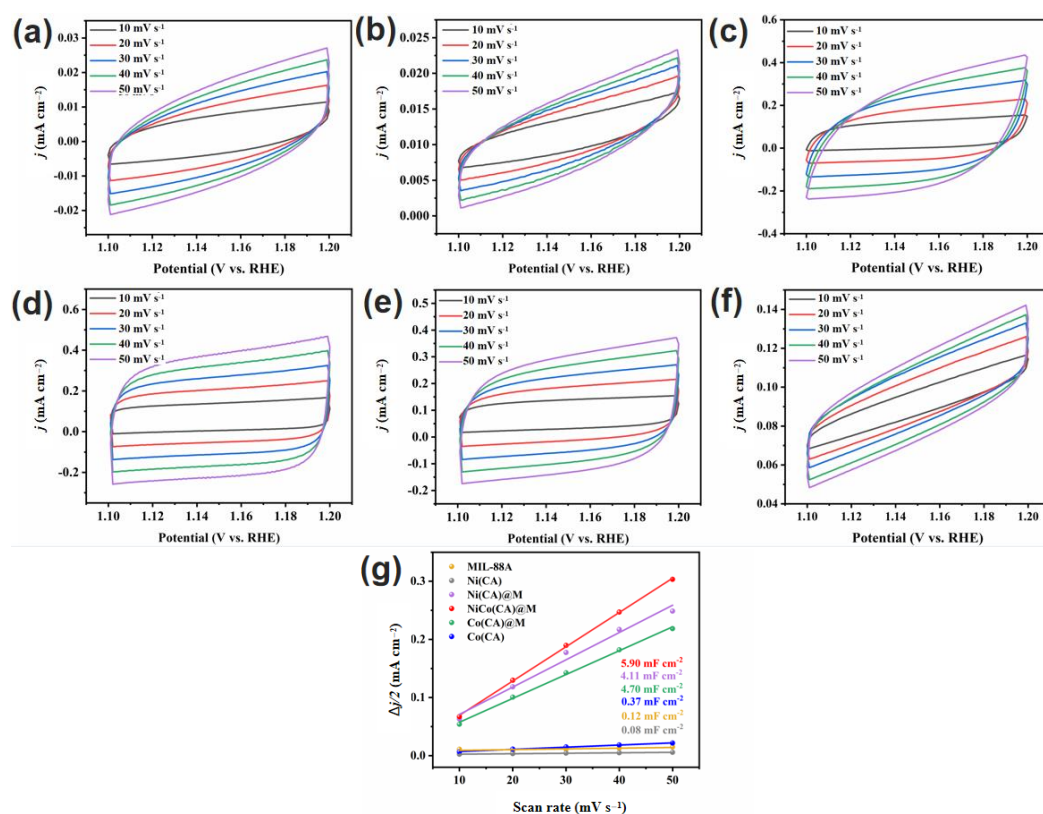

Figure 4. CV curves acquired at the different scanning rates of 10–50 mV s^{-1} from (**a**) MIL-88A, (**b**) Ni(CA), (**c**) Ni(CA)@M, (**d**) NiCo(CA)@M, (**e**) Co(CA)@M, and (**f**) Co(CA). (**g**) The C_{dl} values of MIL-88A, Ni(CA), Ni(CA)@M, NiCo(CA)@M, Co(CA)@M, and Co(CA).

As was known in the previous morphological characterization section, there was a distinct interface between the nickel–cobalt nanoparticles and MIL-88A in the composite. This zero-dimensional/three-dimensional interface can facilitate the effective modulation of the interfacial local electronic structure in the catalytic process and can accelerate the electron transfer, thus enabling the material to exhibit higher electrocatalytic activity. The introduced NiCo(CA) nanoparticles were equivalent to the introduction of new activity.

The rough surface of the exposed additional active sites can also provide more channels to accelerate electron transfer. Electrochemical test results showed that NiCo(CA)@M showed far better electrochemical activity than single components, faster reaction kinetics, larger active specific surface areas, and a smaller charge transfer resistance, and this was consistent with the structural morphological advantages of the composite and the expected results.

Stability is another critical parameter for evaluating the catalyst's performance. The scan rate was set to 10 mV s^{-1} and the NiCo(CA)@M catalyst was subjected to 2000 CV cycles in 1 M KOH, and then the LSV curves before and after the catalyst cycles were tested (Figure 5a) and compared in terms of the overpotential differences at a current density of 50 mA cm^{-2}. The results proved that the overpotential only increased by 6 mV after 2000 CV cycles and still maintained good electrocatalytic activity. The potential was reduced by 23 mV after the 16 h i-t test, which may be due to the surface reconstruction of the catalyst during the i-t test under the conditions of the applied potential, which generated an active structure with better electrocatalytic activity, which also indicates the good durability of the composite. To further explore the long-term stability of this catalyst, a chrono-current test was performed. Figure 5c showed that the NiCo(CA)@M catalyst maintained 91.1% of the initial current density after 16 h of operation at a current density of 10 mA cm^{-2}. Meanwhile, after a 10 h i-test at a high current density of 50 mA cm^{-2}, the current density retention of the NiCo(CA)@M catalyst was 81.9%. This fully indicated that the long-term stability of the NiCo(CA)@M catalyst was excellent. In conclusion, the composite showed good cycling durability and long-term stability.
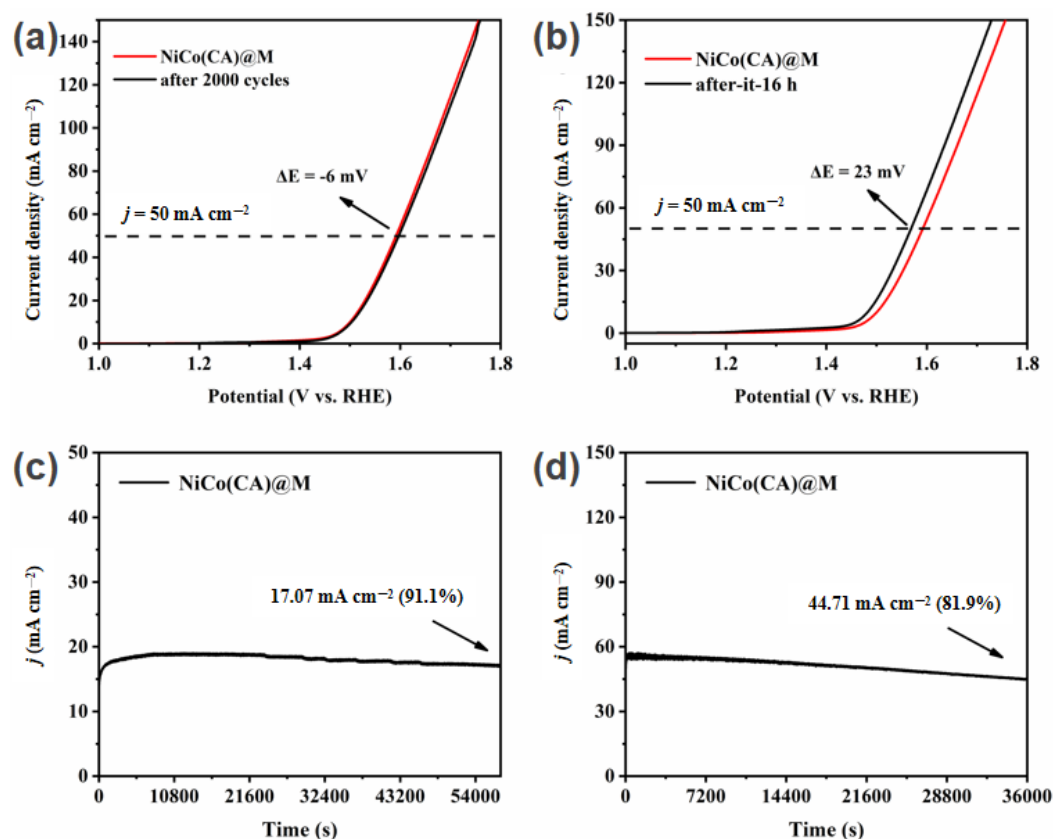

Figure 5. (**a**) Polarization curves of NiCo(CA)@M before and after 2000 cycles. (**b**) Polarization curves of NiCo(CA)@M before and after the i-t stability test. (**c**) Stability test at j = 10 mA cm^{-2} of NiCo(CA)@M. (**d**) Stability test at j = 50 mA cm^{-2} of NiCo(CA)@M.

The in situ growth of nickel–cobalt nanoparticles on the metal-organic framework reduced the agglomeration of nanoparticles and introduced new active sites while giving the catalyst a larger active specific surface area, which provided more channels for the

reaction to accelerate electron transfer and provided more channels for the reaction to accelerate electron transfer. A zero-dimensional/three-dimensional interface was formed in the NiCo(CA)@M catalyst that facilitates the charge redistribution in the material, and this electron transfer can enable the catalyst to show more excellent electrocatalytic activity in the electrocatalytic process. In situ growth makes for a strong interaction between the nickel–cobalt nanoparticles and the metal-organic framework, which lays a good foundation for the excellent stability of the catalyst.

4. Conclusions

In conclusion, NiCo(CA)@M microbars were fabricated using a two-step solvothermal method for in situ growth of nickel–cobalt nanoparticles on the metal-organic framework, and the composites exhibited excellent OER properties. The experimental results show that the composite material has good electrochemical properties with a low overpotential of 270 mV required at 10 mA cm^{-2} and a low Tafel slope of 69 mV dec^{-1}, as well as good durability. The in situ growth of the metal-organic backbone as a substrate solved the problem of the easy agglomeration of nanoparticles. At the same time, the composite material effectively increases and exposes more active sites, and more electron transfer occurs internally, which effectively regulates the charge distribution and has good reaction kinetics. The interfacial interaction between NiCo(CA)@M and the electrode/electrolyte also helps to accelerate the charge transfer between the catalyst and the electrode/electrolyte to improve the conductivity, while the in situ growth of nickel–cobalt nanoparticles on the metal-organic skeleton further enhances the durability and stability of the catalyst.

Supplementary Materials: The following supporting information can be downloaded at https: //www.mdpi.com/article/10.3390/pr11071874/s1. Figure S1: locally enlarged TEM images of NiCo(CA)@M. Figure S2: EDS spectrum of NiCo(CA)@M. Figure S3: XPS survey spectrum for NiCo(CA)@M. Table S1: the energy dispersion spectrum(EDS) element analysis results of NiCo(CA)@M. Table S2: impedance fitting data Rct for MIL-88A, Ni(CA), Ni(CA)@M, NiCo(CA)@M, Co(CA)@M, and Co(CA). Table S3: comparison of the activity for the NiCo(CA)@M catalyst with recently reported electrocatalysts in alkaline electrolyte (see Refs. [27,36,41–44,47–53]).

Author Contributions: J.L.: data curation, writing—original draft. X.W.: data curation, visualization. Y.M. and Q.L.: conceptualization, methodology, writing—review and editing, funding acquisition. Q.X.: supervision, writing—review and editing, project administration, and funding acquisition. All authors have read and agreed to the published version of the manuscript.

Data Availability Statement: Not applicable.

Conflicts of Interest: The authors declare no conflict of interest.

References

1. Razmjoo, A.; Gandomi, A.H.; Pazhoohesh, M.; Mirjalili, S.; Rezaei, M. The key role of clean energy and technology in smart cities development. *Energy Strat. Rev.* **2022**, *44*, 100943. [CrossRef]
2. Wang, J.; Hu, Y.; Wang, F.; Yan, Y.; Chen, Y.; Shao, M.; Wu, Q.; Zhu, S.; Diao, G.; Chen, M. Development of copper foam-based composite catalysts for electrolysis of water and beyond. *Sustain. Energy Fuels* **2023**, *7*, 1604–1626. [CrossRef]
3. Dos Santos, K.G.; Eckert, C.T.; De Rossi, E.; Bariccatti, R.A.; Frigo, E.P.; Lindino, C.A.; Alves, H.J. Hydrogen production in the electrolysis of water in Brazil, a review. *Renew. Sustain. Energy Rev.* **2017**, *68*, 563–571. [CrossRef]
4. Fereja, S.L.; Li, P.; Zhang, Z.; Guo, J.; Fang, Z.; Li, Z.; He, S.; Chen, W. W-doping induced abundant active sites in a 3D NiS2/MoO2 heterostructure as an efficient electrocatalyst for urea oxidation and hydrogen evolution reaction. *Chem. Eng. J.* **2022**, *432*, 134274. [CrossRef]
5. Iqbal, S.; Safdar, B.; Hussain, I.; Zhang, K.; Chatzichristodoulou, C. Trends and Prospects of Bulk and Single-Atom Catalysts for the Oxygen Evolution Reaction. *Adv. Energy Mater.* **2023**, *13*, 1. [CrossRef]
6. Shan, Y.; Sun, X.; Wang, Y.; Zhu, Y.; Li, T. Semimetallic Orbital Hybridization by Particular Surface Engineering in Ternary Cobalt Silicide to Accelerate Oxygen Evolution Reaction. *Phys. Status Solidi Rapid Res. Lett.* **2023**, *17*, 2200445. [CrossRef]

7. Jung, H.B.; Kim, Y.; Lim, J.; Cho, S.; Seo, M.; Kim, I.-S.; Kim, M.; Lee, C.; Lee, Y.-W.; Yoo, C.-Y.; et al. ZIF-67 metal-organic frameworks synthesized onto CNT supports for oxygen evolution reaction in alkaline water electrolysis. *Electrochim. Acta* **2023**, *439*, 2200445. [CrossRef]

8. Li, H.; Guo, Z.; Wang, X. Atomic-layer-deposited ultrathin Co_9S_8 on carbon nanotubes: An efficient bifunctional electrocatalyst for oxygen evolution/reduction reactions and rechargeable Zn-air batteries. *J. Mater. Chem. A* **2017**, *5*, 21353–21361. [CrossRef]

9. Qin, C.; Tian, S.; Wang, W.; Jiang, Z.-J.; Jiang, Z. Advances in platinum-based and platinum-free oxygen reduction reaction catalysts for cathodes in direct methanol fuel cells. *Front. Chem.* **2022**, *10*, 1073566. [CrossRef]

10. Hu, S.; Ge, S.; Liu, H.; Kang, X.; Yu, Q.; Liu, B. Low-Dimensional Electrocatalysts for Acidic Oxygen Evolution: Intrinsic Activity, High Current Density Operation, and Long-Term Stability. *Adv. Funct. Mater.* **2022**, *32*, 2201726. [CrossRef]

11. Tan, D.; Xiong, H.; Zhang, T.; Fan, X.; Wang, J.; Xu, F. Recent progress in noble-metal-free electrocatalysts for alkaline oxygen evolution reaction. *Front. Chem.* **2022**, *10*, 1071274. [CrossRef]

12. Rai, R.K.; Tyagi, D.; Gupta, K.; Singh, S.K. Activated nanostructured bimetallic catalysts for C–C coupling reactions: Recent progress. *Catal. Sci. Technol.* **2016**, *6*, 3341–3361. [CrossRef]

13. Guo, J.; Huo, J.; Liu, Y.; Wu, W.; Wang, Y.; Wu, M.; Liu, H.; Wang, G. Nitrogen-Doped Porous Carbon Supported Nonprecious Metal Single-Atom Electrocatalysts: From Synthesis to Application. *Small Methods* **2019**, *3*, 1900159. [CrossRef]

14. Zhu, B.; Wan, T.; Li, J.; Meng, C.; Du, X.; Liu, G.; Guan, Y. Graphene-wrapped bimetallic nanoparticles bifunctional electrocatalyst for rechargeable Zn-air battery. *J. Electroanal. Chem.* **2022**, *927*, 116946. [CrossRef]

15. Yan, H.; Xiang, H.; Liu, J.; Cheng, R.; Ye, Y.; Han, Y.; Yao, C. The Factors Dictating Properties of Atomically Precise Metal Nanocluster Electrocatalysts. *Small* **2022**, *18*, e2200812. [CrossRef]

16. Ruan, B.; Guo, H.-P.; Hou, Y.; Liu, Q.; Deng, Y.; Chen, G.; Chou, S.-L.; Liu, H.-K.; Wang, J.-Z. Carbon-Encapsulated Sn@N-Doped Carbon Nanotubes as Anode Materials for Application in SIBs. *ACS Appl. Mater. Interfaces* **2017**, *9*, 37682–37693. [CrossRef]

17. Linke, J.; Rohrbach, T.; Ranocchiari, M.; Schmidt, T.J.; Fabbri, E. Enlightening the journey of metal-organic framework (derived) catalysts during the oxygen evolution reaction in alkaline media via operando X-ray absorption spectroscopy. *Curr. Opin. Electrochem.* **2021**, *30*, 100845. [CrossRef]

18. Zha, X.; Zhao, X.; Webb, E.; Khan, S.U.; Wang, Y. Beyond Pristine Metal-Organic Frameworks: Preparation of Hollow MOFs and Their Composites for Catalysis, Sensing, and Adsorption Removal Applications. *Molecules* **2023**, *28*, 144. [CrossRef]

19. Meng, S.; Li, G.; Wang, P.; He, M.; Sun, X.; Li, Z. Rare earth-based MOFs for photo/electrocatalysis. *Mater. Chem. Front.* **2023**, *7*, 806–827. [CrossRef]

20. Luo, P.; Li, S.; Zhao, Y.; Ye, G.; Wei, C.; Hu, Y.; Wei, C. In-situ Growth of a Bimetallic Cobalt-Nickel Organic Framework on Iron Foam: Achieving the Electron Modification on a Robust Self-supported Oxygen Evolution Electrode. *ChemCatChem* **2019**, *11*, 6061–6069. [CrossRef]

21. Ling, J.-L.; Wu, C.-D. Transformation of metal–organic frameworks with retained networks. *Chem. Commun.* **2022**, *58*, 8602–8613. [CrossRef]

22. Wen, M.; Cui, Y.; Kuwahara, Y.; Mori, K.; Yamashita, H. Non-Noble-Metal Nanoparticle Supported on Metal-Organic Framework as an Efficient and Durable Catalyst for Promoting H_2 Production from Ammonia Borane under Visible Light Irradiation. *ACS Appl. Mater. Interfaces* **2016**, *8*, 21278–21284. [CrossRef]

23. Wang, Y.; Liu, J.; Yuan, H.; Liu, F.; Hu, T.; Yang, B. Strong Electronic Interaction between Amorphous MnO_2 Nanosheets and Ultrafine Pd Nanoparticles toward Enhanced Oxygen Reduction and Ethylene Glycol Oxidation Reactions. *Adv. Funct. Mater.* **2023**, *33*, 2011909. [CrossRef]

24. Xiao, M.; Zhu, J.; Li, S.; Li, G.; Liu, W.; Deng, Y.-P.; Bai, Z.; Ma, L.; Feng, M.; Wu, T.; et al. 3d-Orbital Occupancy Regulated Ir-Co Atomic Pair Toward Superior Bifunctional Oxygen Electrocatalysis. *ACS Catal.* **2021**, *11*, 8837–8846. [CrossRef]

25. Wu, W.; Chen, R.; Chen, S.; Wang, Z.; Cheng, N. Optimizing d-Orbital Electronic Configuration via Metal-Metal Oxide Core-Shell Charge Donation for Boosting Reversible Oxygen Electrocatalysis. *Small* **2023**, *19*, e2300621. [CrossRef]

26. Yaqoob, L.; Noor, T.; Iqbal, N.; Nasir, H.; Zaman, N.; Talha, K. Electrochemical synergies of Fe–Ni bimetallic MOF CNTs catalyst for OER in water splitting. *J. Alloy. Compd.* **2021**, *850*, 156583. [CrossRef]

27. Zhang, Q.; Han, P.; Zhang, H.; Yao, J.; Wang, X.; Chen, D.; Zuo, X.; Yang, Q.; Jin, S.; Li, G. Enhanced Oxygen Evolution Activity Aroused from Interfacial Electron Transfer and Synergism in $Co(OH)_2$/MIL-88A Heterostructure. *J. Electrochem. Soc.* **2022**, *169*, 106518. [CrossRef]

28. Bagherzadeh, E.; Zebarjad, S.M.; Hosseini, H.R.M. Morphology Modification of the Iron Fumarate MIL-88A Metal-Organic Framework Using Formic Acid and Acetic Acid as Modulators. *Eur. J. Inorg. Chem.* **2018**, *2018*, 1909–1915. [CrossRef]

29. Khandelwal, G.; Raj, N.P.M.J.; Vivekananthan, V.; Kim, S.-J. Biodegradable metal-organic framework MIL-88A for triboelectric nanogenerator. *iScience* **2021**, *24*, 102064. [CrossRef]

30. Islam, D.A.; Barman, K.; Jasimuddin, S.; Acharya, H. Ag-Nanoparticle-Anchored rGO-Coated MIL-88B(Fe) Hybrids as Robust Electrocatalysts for the Highly Efficient Oxygen Evolution Reaction at Neutral pH. *Chemelectrochem* **2017**, *4*, 3110–3118. [CrossRef]

31. Song, G.; Wang, Z.; Wang, L.; Li, G.; Huang, M.; Yin, F. Preparation of MOF(Fe) and its catalytic activity for oxygen reduction reaction in an alkaline electrolyte. *Chin. J. Catal.* **2014**, *35*, 185–195. [CrossRef]

32. Xie, Q.; Li, F.; Guo, H.; Wang, L.; Chen, Y.; Yue, G.; Peng, D.-L. Template-Free Synthesis of Amorphous Double-Shelled Zinc–Cobalt Citrate Hollow Microspheres and Their Transformation to Crystalline $ZnCo_2O_4$ Microspheres. *ACS Appl. Mater. Interfaces* **2013**, *5*, 5508–5517. [CrossRef] [PubMed]

33. Septiani, N.L.W.; Kaneti, Y.V.; Fathoni, K.B.; Kani, K.; Allah, A.E.; Yuliarto, B.; Nugraha; Dipojono, H.K.; Alothman, Z.A.; Golberg, D.; et al. Self-Assembly of Two-Dimensional Bimetallic Nickel–Cobalt Phosphate Nanoplates into One-Dimensional Porous Chainlike Architecture for Efficient Oxygen Evolution Reaction. *Chem. Mater.* **2020**, *32*, 7005–7018. [CrossRef]

34. Chen, D.; Wang, Y.; Lin, Z.; Huang, F. The pH-dependent binding of zinc citrate to bipy/phen (bipy=2,2-bipyridine, phen=1,10-phenanthroline). *J. Mol. Struct.* **2010**, *966*, 59–63. [CrossRef]

35. Zhang, S.; Zhang, X.; Shi, X.; Zhou, F.; Wang, R.; Li, X. Facile fabrication of ultrafine nickel -iridium alloy nanoparticles/graphene hybrid with enhanced mass activity and stability for overall water splitting. *J. Energy Chem.* **2020**, *49*, 166–173. [CrossRef]

36. Jiang, J.; Huang, L.; Liu, X.; Ai, L. Bioinspired Cobalt-Citrate Metal-Organic Framework as an Efficient Electrocatalyst for Water Oxidation. *ACS Appl. Mater. Interfaces* **2017**, *9*, 7193–7201. [CrossRef]

37. Wang, S.; Hou, Y.; Wang, X. Development of a Stable $MnCo_2O_4$ Cocatalyst for Photocatalytic CO_2 Reduction with Visible Light. *ACS Appl. Mater. Interfaces* **2015**, *7*, 4327–4335. [CrossRef]

38. Kibsgaard, J.; Tsai, C.; Chan, K.; Benck, J.D.; Nørskov, J.K.; Abild-Pedersen, F.; Jaramillo, T.F. Designing an improved transition metal phosphide catalyst for hydrogen evolution using experimental and theoretical trends. *Energy Environ. Sci.* **2015**, *8*, 3022–3029. [CrossRef]

39. Yan, L.; Cao, L.; Dai, P.; Gu, X.; Liu, D.; Li, L.; Wang, Y.; Zhao, X. Metal-Organic Frameworks Derived Nanotube of Nickel-Cobalt Bimetal Phosphides as Highly Efficient Electrocatalysts for Overall Water Splitting. *Adv. Funct. Mater.* **2017**, *27*, 1703455. [CrossRef]

40. Zhang, Y.; Huang, H.; Han, Y.; Qin, Y.; Nie, N.; Cai, W.; Zhang, X.; Li, Z.; Lai, J.; Wang, L. Constructing stable charge redistribution through strong metal-support interaction for overall water splitting in acidic solution. *J. Mater. Chem. A* **2022**, *10*, 13241–13246. [CrossRef]

41. Guo, Y.; Huang, Q.; Ding, J.; Zhong, L.; Li, T.-T.; Pan, J.; Hu, Y.; Qian, J.; Huang, S. CoMo carbide/nitride from bimetallic MOF precursors for enhanced OER performance. *Int. J. Hydrogen Energy* **2021**, *46*, 22268–22276. [CrossRef]

42. Li, F.; Li, J.; Zhou, L.; Dai, S. Enhanced OER performance of composite Co-Fe-based MOF catalysts via a one-pot ultrasonic-assisted synthetic approach. *Sustain. Energy Fuels* **2021**, *5*, 1095–1102. [CrossRef]

43. Zhou, J.; Han, Z.; Wang, X.; Gai, H.; Chen, Z.; Guo, T.; Hou, X.; Xu, L.; Hu, X.; Huang, M.; et al. Discovery of Quantitative Electronic Structure-OER Activity Relationship in Metal-Organic Framework Electrocatalysts Using an Integrated Theoretical-Experimental Approach. *Adv. Funct. Mater.* **2021**, *31*, 1–13. [CrossRef]

44. Wang, D.; Zhang, Y.; Fei, T.; Mao, C.; Song, Y.; Zhou, Y.; Dong, G. NiCoP/NF 1D/2D Biomimetic Architecture for Markedly Enhanced Overall Water Splitting. *Chemelectrochem* **2021**, *8*, 3064–3072. [CrossRef]

45. Tasviri, M.; Shekarabi, S.; Taherinia, D.; Zare Pour, M.A. Nanosized $NiFeSe_2/NiCo_2O_4$ hierarchical arrays on Ni foam as an advanced electrocatalyst for hydrogen generation. *Sustain. Energy Fuels* **2022**, *7*, 112–121. [CrossRef]

46. Cai, K.; Zuo, S.; Luo, S.; Yao, C.; Liu, W.; Ma, J.; Mao, H.; Li, Z. Preparation of polyaniline/graphene composites with excellent anti-corrosion properties and their application in waterborne polyurethane anticorrosive coatings. *RSC Adv.* **2016**, *6*, 95965–95972. [CrossRef]

47. Wang, A.-L.; Xu, H.; Li, G.-R. NiCoFe Layered Triple Hydroxides with Porous Structures as High-Performance Electrocatalysts for Overall Water Splitting. *ACS Energy Lett.* **2016**, *1*, 445–453. [CrossRef]

48. Hou, G.; Jia, X.; Kang, H.; Qiao, X.; Liu, Y.; Li, Y.; Wu, X.; Qin, W. CoNi nano-alloys modified yolk-shell structure carbon cage via Saccharomycetes as carbon template for efficient oxygen evolution reaction. *Appl. Catal. B Environ.* **2022**, *315*, 121551. [CrossRef]

49. Yan, X.; Li, K.; Lyu, L.; Song, F.; He, J.; Niu, D.; Liu, L.; Hu, X.; Chen, X. From Water Oxidation to Reduction: Transformation from $Ni_xCo_{3-x}O_4$ Nanowires to NiCo/NiCoOx Heterostructures. *ACS Appl. Mater. Interfaces* **2016**, *8*, 3208–3214. [CrossRef]

50. Lim, D.; Oh, E.; Lim, C.; Shim, S.E.; Baeck, S.-H. Bimetallic NiFe alloys as highly efficient electrocatalysts for the oxygen evolution reaction. *Catal. Today* **2020**, *352*, 27–33. [CrossRef]

51. Kiran, S.; Yasmeen, G.; Shafiq, Z.; Abbas, A.; Manzoor, S.; Hussain, D.; Pashameah, R.A.; Alzahrani, E.; Alanazi, A.K.; Ashiq, M.N. Nickel-based nitrodopamine MOF and its derived composites functionalized with multi-walled carbon nanotubes for efficient OER applications. *Fuel* **2023**, *331*, 125881. [CrossRef]

52. Gaur, A.; Pundir, V.; Krishankant; Rai, R.; Kaur, B.; Maruyama, T.; Bera, C.; Bagchi, V. Interfacial interaction induced OER activity of MOF derived superhydrophilic Co_3O_4-NiO hybrid nanostructures. *Dalton T.* **2022**, *51*, 2019–2025. [CrossRef] [PubMed]

53. Kang, T.; Kim, J. Optimal cobalt-based catalyst containing high-ratio of oxygen vacancy synthesized from metal-organic-framework (MOF) for oxygen evolution reaction (OER) enhancement. *Appl. Surf. Sci.* **2021**, *560*, 150035. [CrossRef]